Materials Horizons

ROYAL SOCIETY OF CHEMISTRY

COMMUNICATION

View Article Online
View Journal | View Issue

Cite this: *Mater. Horiz.*, 2025, **12**, 8122

Received 22nd April 2025,
Accepted 26th June 2025

DOI: 10.1039/d5mh00756a

rsc.li/materials-horizons

Enhanced photocatalytic gold recovery with concurrent near-IR fluorescence turn-on sensing: N,S-doped CDs in functionalized dendritic silica as a dual-mode platform†

Sanjay Yadav,*[ac] Nishu Choudhary,[ac] Vasavdutta Sonpal[bc] and Alok Ranjan Paital *[ac]

The concurrent gold detection and extraction in aqueous medium is crucial for gold exploration and resource recovery. While using a single material for dual purposes offers distinct advantages, it remains relatively underexplored. This study introduces a rationally engineered heterojunction material that enables selective fluorescence-based turn-on gold detection in the near-IR region, coupled with photocatalytic enhanced adsorption. The hybrid composite material (NSCD@DFNS@BMB-AO) consists of dendritic fibrous silica integrated with *in situ* grown N,S-doped carbon dots (NSCDs) as a fluorescence indicator in the silica matrix and covalently attached amidoxime ligands for gold binding. The incorporation of NSCDs enables photoluminescence in near-IR regions while also promoting photocatalytic activity. The material uniquely enables turn-on gold-ion detection in the near-IR region through photoinduced electron transfer (PET) disruption, offering an ultra-low detection limit (LOD) of 9.9 nM with excellent selectivity. The adsorption potential of the material (780 mg g^{-1}) was enhanced through the photocatalytic reduction of Au(III) to Au(0). Furthermore, the ROS (reactive oxygen species) activity contributes to the material's antimicrobial properties, which are essential to prevent biofouling in aquatic environments. With its rapid response, fast kinetics, effective adsorption capability, and nearly complete gold recovery (~98%) from e-waste, this material demonstrates significant potential for gold extraction and recovery.

New concepts

In this manuscript, we present a rationally designed silica-based composite material capable of simultaneously detecting and adsorbing gold from aqueous environments, while also exhibiting anti-biofouling properties. Although metal–organic frameworks (MOFs) and covalent organic frameworks (COFs) have been explored for dual gold detection and extraction, largely due to their intrinsic fluorescence, functional silica materials remain relatively underexplored for such applications. Our approach integrates dendritic silica with *in situ* grown N,S-doped carbon dots (NSCDs), imparting near-infrared (NIR) luminescence and photocatalytic activity. This design effectively mitigates the common aggregation issues associated with carbon dots and achieves excitation-independent emission. Further modification with amidoxime ligands enhances the material's gold-binding affinity. Notably, this system enables rare fluorescence turn-on detection of gold ions in the NIR region and facilitates photocatalytic reduction of Au(III), significantly boosting gold adsorption capacity, demonstrating practical potential for efficient gold recovery from e-waste. Additionally, the generation of reactive oxygen species (ROS) imparts antimicrobial properties, helping prevent biofouling in aquatic settings. Overall, this study serves as a proof-of-concept for the rational design of multifunctional materials, showcasing the synergy of tailored components in delivering diverse functionalities within a single platform.

1. Introduction

Gold, a noble metal with its unique physical and chemical properties, is indeed an indispensable element shaping both the history and the modern world. It plays a crucial role across various domains, including electronics, catalysis, electrochemistry, nanotechnology, and jewelry.[1–4] However, the disparity in demand and supply has led to overexploitation of conventional and secondary sources.[5,6] Despite high economic and technological value, gold extraction can have adverse environmental impacts, leading to gold ion contamination in water and soil, posing risks to aquatic organisms and human health.[7–9] These compounds can induce oxidative stress and disrupt cellular processes in living organisms, making their accumulation in wastewater a serious concern.[10,11] Also, detecting gold in aqueous bodies is an indicator for gold exploration in surrounding soil or rocks. In industrial settings, detecting gold in wastewater indicates material losses or inefficient extraction processes. Thus, the detection of gold in aqueous medium is

[a] *Salt and Marine Chemicals Division, CSIR-Central Salt & Marine Chemicals Research Institute, G.B Marg, Bhavnagar-364002, Gujarat, India. E-mail: arpaital@csmcri.res.in, alokpaital@gmail.com, sychem00700@gmail.com*
[b] *Analytical and Environmental Science Division & Centralized Instrument Facility, CSIR-Central Salt & Marine Chemicals Research Institute, G.B Marg, Bhavnagar-364002, Gujarat, India*
[c] *Academy of Scientific and Innovative Research (AcSIR), Ghaziabad-201002, India*

† Electronic supplementary information (ESI) available. See DOI: https://doi.org/10.1039/d5mh00756a

crucial for environmental protection, resource recovery, and economic benefits, making it an indispensable tool in modern and environmental practices. Conventional gold ion detection methods face challenges like low sensitivity, toxicity, and complex procedures.[12,13] In contrast, fluorescence-based sensing offers a simpler, cost-effective, and highly sensitive alternative.[14,15] Reusable heterogeneous probes are now preferred over traditional organic probes.[16–19] Most detection studies report fluorescence quenching by Au^{3+} in the blue or green regions. However, turn-on fluorescence sensing in the near-IR (NIR) region offers key advantages such as reduced background interference, lower phototoxicity, and higher sensitivity, which is ideal for environmental monitoring.[20] NIR sensing provides clearer signals due to minimal interference from visible light and compatibility with both organic and aqueous media.[21] With ongoing advances in nanomaterials, NIR-based sensors are poised to become essential tools for the selective and sensitive detection of gold ions. To the best of our knowledge, there is currently no report on nanomaterial-based near-IR turn-on detection of gold ions.

Similarly, gold extraction is crucial for both economic and environmental reasons. While traditionally sourced from natural ore, concerns over resource scarcity and environmental impact have shifted focus to secondary sources.[22] E-waste, the fastest-growing solid waste stream, reached 52 million metric tons in 2019 and contains valuable metals like gold.[23] Although oceans hold large amounts of gold, extraction is hindered by low concentrations and ion competition.[24] Thus, innovative methods for recovering gold from e-waste are vital for sustainability. At present, methods for extracting gold from electronic waste predominantly involve chemical precipitation,[25,26] electrochemical reduction,[27] solvent extraction,[28] and chemical/physical adsorption.[29,30] Among these methods, adsorption is a widely accepted, economical, energy-efficient, and sustainable approach for recovering gold ions.[30,31] However, conventional adsorbents such as activated carbon, inorganic, and biomaterials are inefficient in the recovery process offering poor selectivity and low adsorption capacity.[32–35] Efforts have been made to improve selectivity and adsorption capacity towards gold ions by developing novel gold selective adsorbents such as covalent organic frameworks (COFs),[36–39] metal–organic frameworks (MOFs),[30,40–44] porous polymers (POPs),[45–48] PAN fibers,[49] cryogels,[50] and polymeric films.[51] Literature reports indicate that adsorption performances of various adsorbents depend on the effective surface area, pore size, binding sites, and the presence of photo- and redox-active centres. Therefore, in recent times, the incorporation of photoactive centres in adsorbents has emerged as a promising approach for gold recovery, offering a more efficient, rapid, and sustainable process compared to traditional extraction methods.[52–57] This combined method leverages adsorption of gold ions, with concurrent photocatalytic reduction under light irradiation to elemental gold, enhancing the adsorption capacity of the material. Another advantage of photoactive centres in adsorbents is their ability to generate reactive oxygen species (ROS), which helps inhibit biofouling in wastewater environments.[58] Upon a thorough review of the literature, it is evident that considerable attention has been focused on gold recovery, while fewer efforts have been directed toward the development of concurrent detection capabilities. It is also noted that the reported materials designed for dual purposes[15–18,54,59,60] primarily involve MOFs or COFs, due to their inherent fluorescence properties. However, most of these materials exhibit fluorescence quenching primarily in the blue or green regions and lack anti-biofouling capabilities.

Therefore, we aimed to create a hybrid material for fluorescence turn-on gold detection in a higher wavelength regime with concurrent adsorption. The design incorporates a high surface area fibrous mesoporous silica matrix with *in situ* grown photo-active carbon dots, further functionalized with an amidoxime ligand for gold binding. We opted for a fibrous silica matrix due to its favourable characteristics, such as fibrous morphology with high surface area, outstanding aqueous dispersibility, and radial accessibility of pore channels for improved ligand loading.[61–64] Nitrogen and sulphur-doped carbon dots (NSCDs) were selected as fluorescence tags for their near IR signalling capabilities and photocatalytic effects, which could help address biofouling through the generation of reactive oxygen species (ROS) and enhance gold extraction by photocatalytically reducing Au(III) to elemental Au(0).[54,58] The amidoxime-based ligand was chosen for its selective gold binding affinity.[59] Following the design strategy, we synthesized the hybrid material NSCD@DFNS@BMB-AO for concurrent detection and photocatalytic extraction of gold ions. The final material exhibits selective turn-on fluorescence sensing of gold in the near IR region, maintaining high selectivity and minimal interference in the presence of a wide range of cations and anions. This is beneficial since CDs most often exhibit fluorescence quenching with blue luminescence, which limits their practical use in environmental monitoring. However, NSCD@DFNS@BMB-AO, functioning as a luminescent probe, exhibits turn-on, near- IR and excitation-independent emission, making it desirable and well-suited for analysis in environmental and biological samples. Batch adsorption and kinetic studies displayed high gold uptake with rapid kinetics and selective gold extraction from e-waste leached liquor. Additionally, this material demonstrated photocatalytic enhanced gold extraction and anti-microbial activity to resist biofouling of the material. With its recyclability, this material shows promise for a sustainable approach to gold extraction, addressing environmental monitoring and remediation needs while providing an efficient means of harnessing this economic source material.

2. Results and discussion

2.1 Synthetic, structural insights, and surface analysis

Scheme 1 shows the synthetic steps involved in the synthesis of the final material NSCD@DFNS@BMB-AO. The dendritic fibrous nano-silica (DFNS) was synthesized in a biphasic medium (1-octanol + water) using myristyl trimethylammonium bromide as the template, $NaHCO_3$ and triethyl amine as a hydrolyzing agent, TEOS as the silica precursor, and tetrabutyl

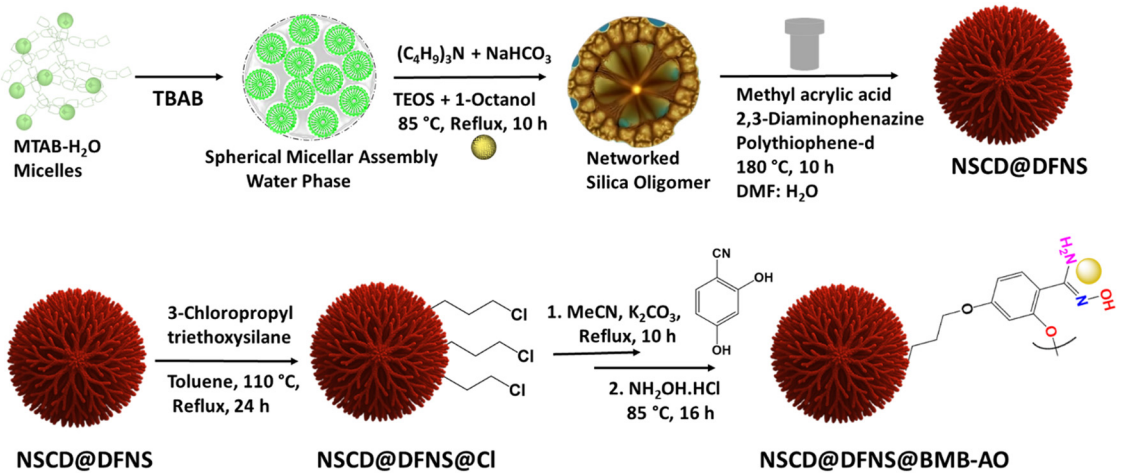

Scheme 1 The synthetic scheme of the materials NSCD@DFNS, NSCD@DFNS@Cl, and the final material NSCD@DFNS@BMB-AO.

ammonium bromide as a phase transfer catalyst. During the silica seeding and aging for 1 h, the carbon dot precursor, methyl acrylic acid as the carbon source, 2,3-diamino phenazine (DAP) as the nitrogen dopant, and poly(3,4-ethylene dioxythiophene) (PEDOT) as the sulfur dopant were hydrothermally heated, resulting in an N,S-doped carbon dot embedded silica nanomaterial, NSCD@DFNS. The optimized conditions are detailed in the ESI† (Table S1 and Fig. S1). This *in situ* growth of CDs is advantageous in addressing the aggregation concerns with CDs and requires no prior purification.[65] The NSCD@DFNS material was further covalently functionalized with 3-CPTES (3-chloropropyltrimethoxysilane) to get the NSCD@DFNS@Cl material, which subsequently reacted with the BMB ligand and finally amidoximated to obtain the final material NSCD@DFNS@BMB-AO. The synthesized materials were characterized to establish their formation, and the final material NSCD@DFNS@BMB-AO was explored for fluorescence detection and simultaneous adsorption studies.

The morphological parameters for NSCD@DFNS, NSCD@DFNS@Cl and NSCD@DFNS@BMB-AO materials were assessed using field-emission scanning electron microscopy (FESEM), transmission electron microscopy (TEM), and high-resolution transmission electron microscopy (HR-TEM) (Fig. 1). The FESEM images of the NSCD@DFNS material revealed highly porous spherical particles (60–90 nm) with clearly visible pores and discrete morphology, which is nearly constant throughout the covalent functionalization process (Fig. 1A–C). The primary evidence of the presence of the N,S doped carbon dots was confirmed using energy dispersive X-ray (EDX) analysis and elemental mapping of the final material (NSCD@DFNS@BMB-AO), showing signals for silicon, oxygen, carbon, nitrogen, and sulfur (Fig. S2, ESI†). The TEM and HR-TEM images confirmed the radial fibrous

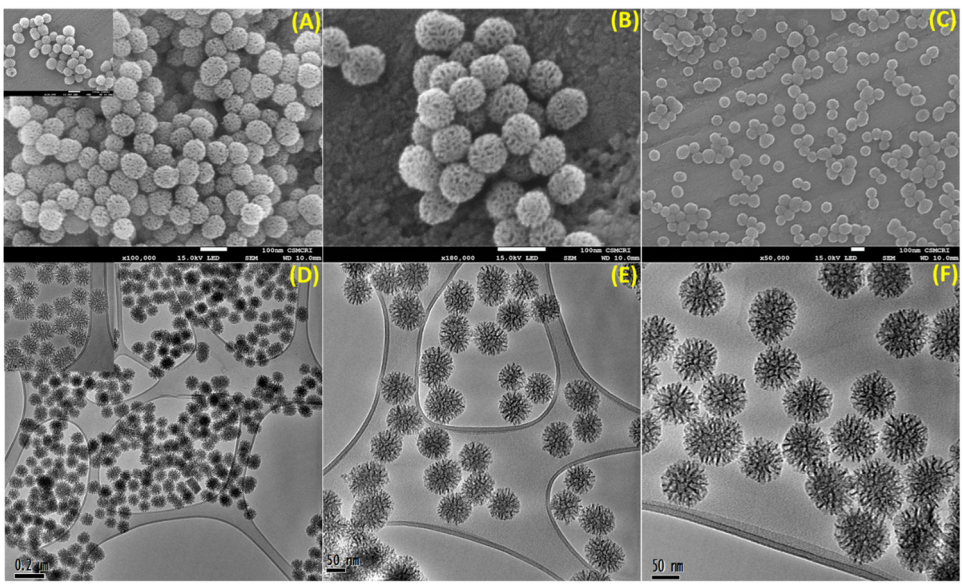

Fig. 1 (A)–(C) The FESEM images of the NSCD@DFNS, NSCD@DFNS@Cl and NSCD@DFNS@BMB-AO materials (scale bar: 100 nm). (D)–(F) The TEM and HR-TEM images of the NSCD@DFNS, NSCD@DFNS@Cl, and the final material NSCD@DFNS@BMB-AO (scale bar: 0.2 μm (inset: 20 nm), 50 nm).

Table 1 The N_2 BET physicochemical parameters

Material type	Surface area ($m^2\ g^{-1}$)	Pore size (nm)	Pore volume ($cm^3\ g^{-1}$)
NSCD@DFNS	1600	21.7, 10.4	2.01
NSCD@DFNS@Cl	890	7.6, 6.5	1.423
NSCD@DFNS@BMB-AO	389	3.9	0.671

morphology of the material with center radial pores having varied dendrimer lengths and gaps estimated to be 25–40 nm and 8–15 nm, which ideally serves for effective functionalization, ensuring high functional organic payloads (Fig. 1D–F). The growth of the radially fibrous silica nanomaterial was meticulously monitored during the nucleation phase, revealing the formation dynamics of a bicontinuous emulsion-assisted synthesis (Fig. S3, ESI†). This process, driven by phase separation and templating mechanisms, led to the emergence of a highly interconnected, branched network of fibrous silica. The physicochemical parameters (Table 1) were obtained using N_2 Brunauer–Emmett–Teller (BET) analysis showing a high surface area of order 1600 $m^2\ g^{-1}$ for NSCD@DFNS with a high pore volume (2 $cm^3\ g^{-1}$) in the mesoporous range with different pore sizes ($\sim$21, 10 nm), which significantly reduced during a successful chemical functionalization process (Fig. S4, ESI†). The materials displayed type IV isotherms, with the highest capillary condensation observed in the initial material (NSCD@DFNS) and the lowest in the final product (NSCD@DFNS@BMB-AO). The amorphous nature of the materials was confirmed by high-angle powder X-ray diffraction (PXRD) showing broad peaks at $\sim$23°, which remain unaltered during the chemical processing (Fig. S5A, ESI†). The thermogravimetric analysis (TGA) profiles of the materials were also assessed to realize the nature and stability of the materials (Fig. S5B, ESI†). The profiles as a function of temperature are divided into 3 phases, phase 1 from (0–250 °C) ascribed to the loss of any form of physically adsorbed water molecules on the surface, which is higher in the final material (NSCD@DFNS@BMB-AO) probably due to a greater extent of hydrogen bonding. Phase 2 (250–550 °C) is ascribed to the organic loss due to chemically attached functionalities, resulting in −22.84%, −29.03%, and −57.42% loss for the starting material NSCD@DFNS, NSCD@DFNS@Cl and the final material NSCD@DFNS@BMB-AO. The increased organic losses observed in the initial material (NSCD@DFNS) compared to traditional mesoporous silica can be attributed to the encapsulated carbon dots within the material. The successive variation in higher organic losses mainly arises from the stepwise surface functionalization process. The higher organic losses compared to the conventional mesoporous materials indicate more organic loading due to unique fibrous morphology with radial channels for effective functionalization in DFNS material. The third phase (550 to 800 °C) indicates the dehydroxylation of surface silanol groups.

The examination and interpretation of the Fourier transform infrared spectroscopy (FTIR) spectra of the materials provided crucial insights into the functional groups present in the silica matrix (Fig. S6, ESI†). For the initial material, NSCD@DFNS, specific peaks were observed at 3433, 2942, 1720, 1625, 1425, 1378, 1642, 1664, 1445, 1215, 1095, 690, and 1079 cm^{-1}, representing vibrations of Si–OH, –OH, C═O stretching, NH, and OH bending functionalities. Additionally, the vibrations at 1215, 1378, 690, 1642, 1664, 1445, 1095, and 1079 cm^{-1} indicated the presence of C–O, C–N, C–S, C═C, C═S, and Si–O–Si functionalities within the material (Fig. S6A, ESI†). These distinct peaks, differing from the silica framework, conclusively confirmed the encapsulation of carbon dots within the silica matrix. The FTIR spectrum of NSCD@DFNS@Cl exhibited additional peaks at 2936, 2883, and 660 cm^{-1}, for alkyl (–CH_2–) and C–Cl stretching vibrations of the 3-CPTES groups, thereby validating the formation of the NSCD@DFNS@Cl material. Moreover, peaks at 3325, 3325, and 2245 cm^{-1} for the NSCD@DFNS@BMB material are attributed to NH and CN stretching vibrations, confirming the successful attachment of the ligand moiety (Fig. S6B, ESI†). The amidoximation process converted the nitrile group (2244 cm^{-1}) into characteristic C═N, C–N, and N–O functionality bands that appeared at 1635, 1379, and 931 cm^{-1} for the final material NSD@DFNS@BMB-AO, also supported by the disappearance of the 2244 cm^{-1} peak in the final material evidencing the successful amidoximation process (Fig. S6C, ESI†). The integrity of the CDs was maintained within the silica matrix throughout the chemical processing (Fig. S6D, ESI†).

Furthermore, X-ray photoelectron spectroscopy (XPS) was employed to examine the surface state properties of the materials (Fig. 2). The chemical synthesis of the initial material, NSCD@DFNS, was scrutinized through full scan and core–shell XPS spectra. In the full scan XPS spectra, signals corresponding to oxygen (O), nitrogen (N), carbon (C), sulfur (S), and silicon (Si) confirmed the integration of carbon dots into the silica matrix (Fig. 2A). The core–shell C 1s spectra were deconvoluted into six peaks representing C–C/C═C (284.5 eV), C–N/C–S (285.4 eV), C–O (286.6 eV), C═S (287.2 eV), C═O (288.2 eV), and O–C–C═O (288.8 eV) functionalities (Fig. 2B). The N 1s spectra were deconvoluted into three peaks at 398.1, 399.2, and 400.2 eV, resembling pyridinic, amino, and pyrrolic nitrogen (N) (Fig. 2C). Similarly, the deconvolution of the O 1s spectrum into two peaks at 532.7 and 534.7 eV confirmed the presence of Si–OH and Si–O–Si framework functionalities (Fig S7A, ESI†). The existence of the silica matrix was confirmed by a full scan spectrum showing a signal for silicon (Si) and a core–shell Si-2p spectra peak at 102.8 eV (Fig. S7B, ESI†). The covalent bonding of 3-CPTES to produce the NSCD@DFNS@Cl material was confirmed by the Cl-2p peak in the comprehensive full scan spectrum and the deconvoluted peak at 200.4 eV of the core–shell Cl spectrum with an intact silica framework (Fig. 2D–F). The ultimate amidoximated product, NSCD@DFNS@BMB-AO, displayed all the necessary elemental peaks post-chemical functionalization with the increased intensity of carbon and nitrogen hinting towards successful chemical processing (Fig. 2G). The C 1s spectrum peaks closely resemble those of the starting material (Fig. S8A, ESI†), while the N 1s spectrum of the final product displays peaks at 398.2, 399.1, 400.2, and 401.1 eV, corresponding to pyridinic, amino, pyrrolic, and oximido N (N–OH) species, suggesting the successful amidoximation process, with the increased peak intensity at 399.2 eV of the

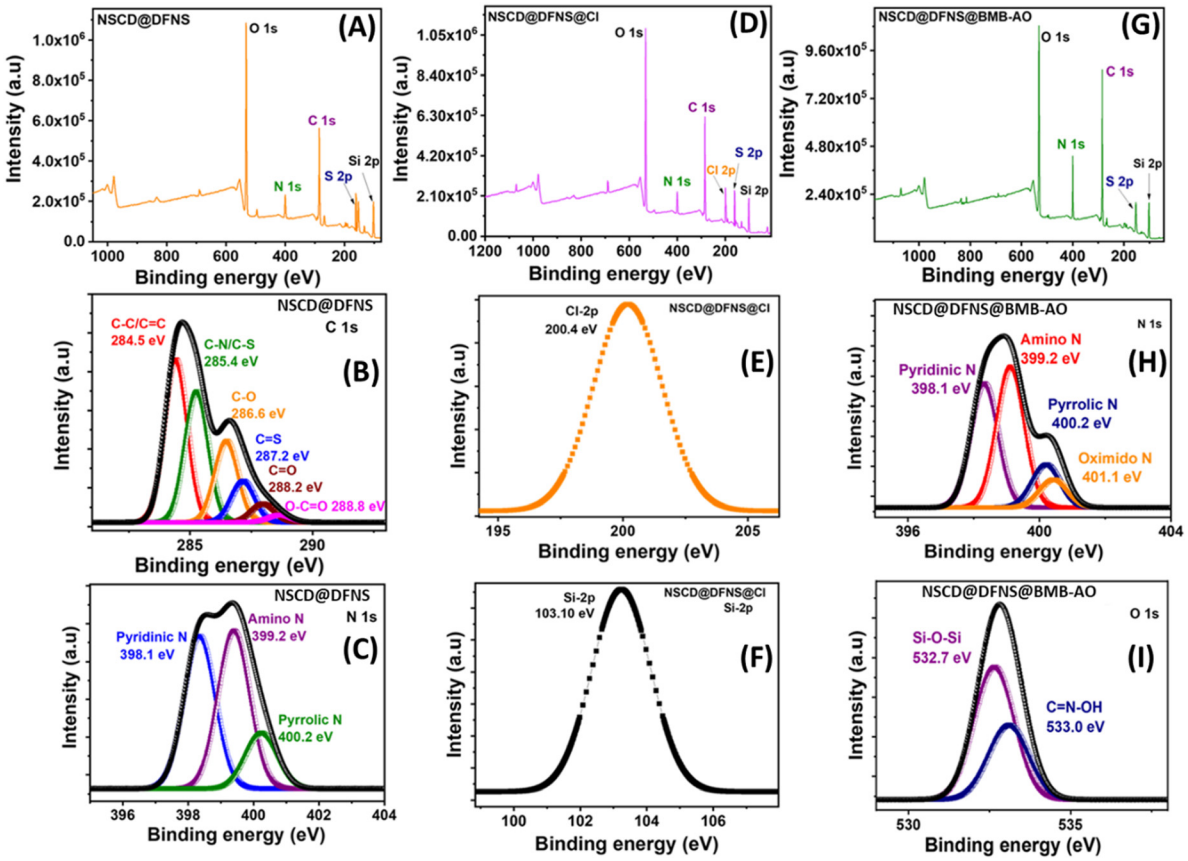

Fig. 2 (A)–(C) The XPS full scan and core–shell C 1s and N 1s spectra of the NSCD@DFNS material. (D) The XPS full scan spectra of the Cl-functionalized material (NSCD@DFNS@Cl). (E) and (F) The XPS core–shell Cl-2p and Si-2p spectra of the Cl-functionalized material (NSCD@DFNS@Cl). (G)–(I) The XPS full scan and the core–shell (N 1s and O 1s) spectra of the final NSCD@DFNS@BMB-AO material.

amino N hinting the prevalence of more surface amino groups post-conversion (Fig. 2H). Similarly, the O 1 spectra revealed peaks at 532.7 and 533.0 eV, attributed to the Si–O–Si network and C═N–OH functionality, providing successful chemical evidence of the amidoximation process while maintaining the silica matrix (Fig. 2I and Fig. S8B, ESI†).

2.2 Optical screening

The final material NSCD@DFNS@BMB-AO was screened for photophysical properties using ultraviolet-visible spectroscopy (UV-Vis) and fluorescence studies in an aqueous buffer medium. Initially, the material exhibited three absorption bands at 450, 516, and 732 nm, likely due to π–π* and n–π* transitions (Fig. S9, ESI†). The fluorescence emission spectrum was recorded with excitations at these characteristic absorption wavelengths and no significant fluorescence emission was observed at 450 and 516 nm excitation wavelengths. However, when excited at 730 nm, the material displayed an intense emission band at 950 nm in the near-infrared (NIR-I) region with significantly enhanced Stokes shift desirable in sensing application (Fig. 3A). The doping of polymerized carbon dots with N and S influences the fluorescence properties of the material. Doping with nitrogen atoms introduces additional lone pairs and π-electrons, creating new electronic states and reducing the band gap. N doping can also facilitate the formation of graphitic N and pyridinic N, modifying energy levels and promoting red-shifted emissions.[66] Sulfur atoms, being larger than carbon, introduce structural distortion and create mid-gap states, thereby reducing the band gap.[67] Apart from the quantum confinement effects, N and S doping can promote emission at higher wavelengths by enhancing π–π* transitions within the polymerized carbon dot structure and facilitating intersystem crossing, effectively contributing to lower energy emissions.[68] Additionally, considering the diverse photoactive nature and multiple surface functional groups of the trapped carbon dots, the excitation-dependent behaviour of the material was also investigated. The material was subjected to different excitation energies near 700 nm, and surprisingly, it showed an excitation-independent response with a constant emission band centred at 950 nm (Fig. S10, ESI†). This excitation-independent emission of the final material is probably due to the fine-tuned *in situ*-controlled growth of carbon dots in the mixed mesopore dendritic channels, offering advantages in practical sensing applications by eliminating the need for multiple excitation sources.

The fluorescence studies were also carried out in the presence of various cations and anions for the selectivity studies (Fig. 3A, B and Fig. S11, ESI†). Among the different cations, the material showed a selective fluorescence response

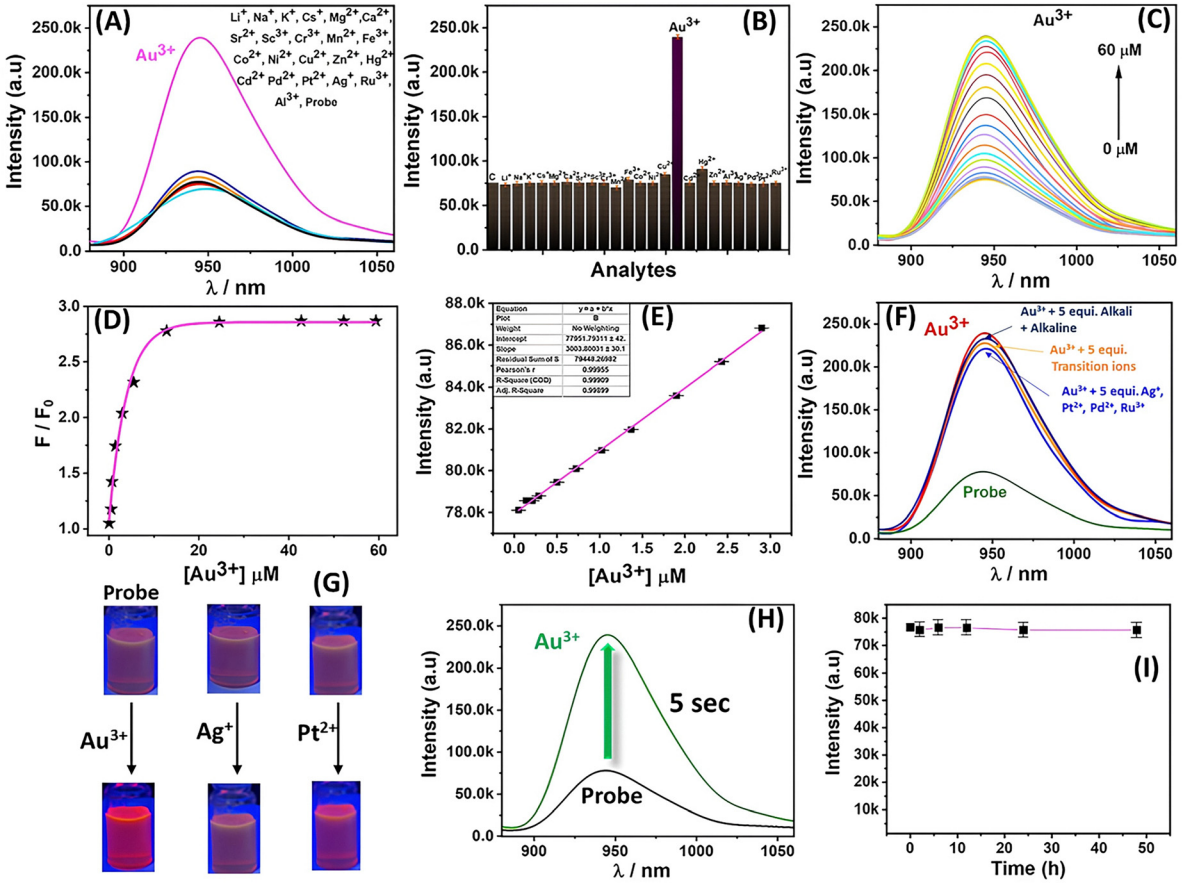

Fig. 3 (A) The fluorescence selectivity screening with various ions. (B) The relative fluorescence emission intensity of the material with different cations. (C) The titration profile with the Au^{3+} ions. (D) The non-linear binding plot with Au^{3+} ions. (E) The LOD (limit of detection) plot. (F) The interference study plot of the material with an excess of alkali, alkaline, transition, and precious metal ions. (G) The pictures of the probe material (long-wave UV; 365 nm) before and after the addition of Au^{3+}, Ag^{+}, and Pt^{2+} ions. (H) The fast response behaviour of the material toward Au^{3+} ions. (I) The plot fluorescence emission stability with respect to time.

towards Au^{3+} ions, with an increase in the emission intensity, demonstrating a turn-on behavior. In contrast, no fluorescence changes were observed with other ions, confirming the material selectivity for Au^{3+} ions. To gain further insights, fluorescence titration was performed with increasing concentrations of Au^{3+} ions (Fig. 3C). The fluorescence titration up to saturation concentration provided the fluorescence enhancement constant, following a non-linear equation (Fig. 3D).[69] The limit of detection (LOD),[70] limit of quantification (LOQ), and linear range parameters were derived from the successive addition of low concentration Au^{3+} ions and were calculated using the 3σ and 10σ methods, which were 9.9 nM, 33.29 nM and 0.033–3 μM respectively[71] (Fig. 3E and Fig. S12, ESI†). The interference behavior was also examined, showing the material's ultra-selectivity in the presence of excess other ions and similar group elements like Ag, Pt, Pd, and Ru, with a fast response behaviour (Fig. 3F–H). The fluorescence emission stability in the dispersion medium was monitored, showing good intact emission stability over time (Fig. 3I). Additionally, pH-dependent optical emission and structural stability were also investigated, where the material showed stable emission intensity and excellent structural integrity in different pH ranges (Fig. S13, ESI†). However, minor fluorescence quenching was observed under highly acidic conditions after prolonged exposure time.

2.3 Sensing mechanism

Heteroatom doping plays a crucial role in altering the photophysical properties of carbon dots (CDs), allowing them to act as both electron donors and acceptors. Specifically, introducing nitrogen and sulfur (NS-CDs) into the sp^2 carbon framework significantly alters the photophysical behavior of CDs, enhancing their charge transfer dynamics and sensitivity. In our study, we noted a clear turn-on fluorescence response to gold ions, a phenomenon not commonly observed in CD-based confined porous materials (Fig. 4). Initially, the nitrogen and oxygen donor functional groups in the material serve as electron donors, promoting a photoinduced electron transfer (PET) process. This electron transfer interferes with radiative recombination, leading to a reduced fluorescence intensity of the material (Fig. 4A and B). However, when gold ions are introduced, the electron-deficient gold ions coordinate with the donor sites, effectively suppressing PET and restoring

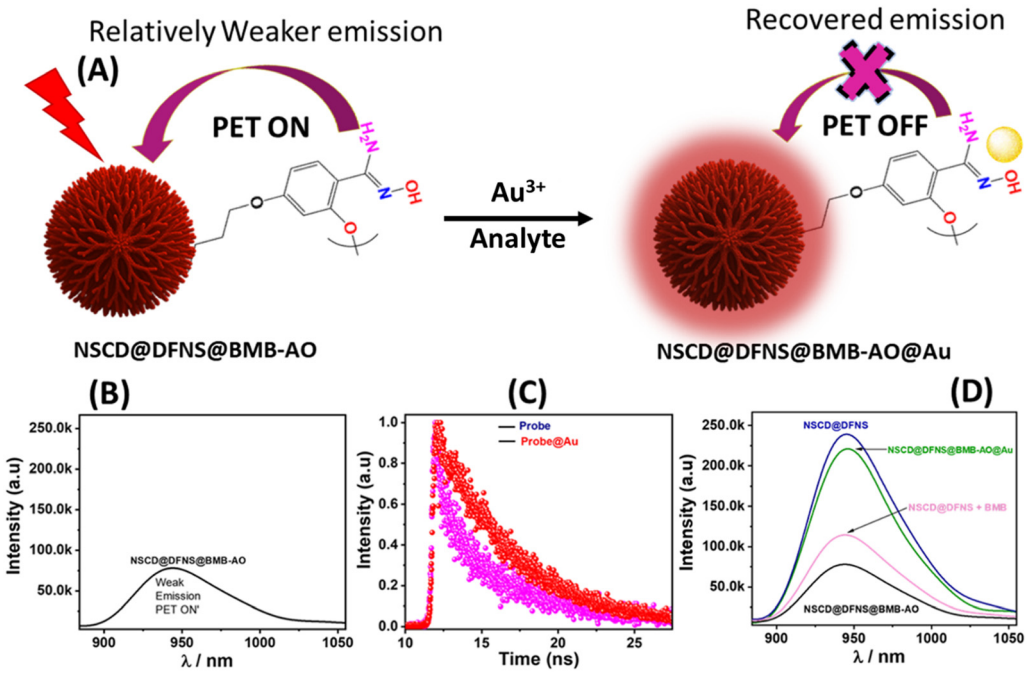

Fig. 4 (A) The schematic representation of the turn-off–on sensing behaviour of the material driven by the PET on–off mechanism towards gold ions. (B) The fluorescence emission response of the probe material without gold ions. (C) The time-correlated single photon counting (TCSPC) profile of the material before and after the addition of Au^{3+} ions. (D) The fluorescence emission of the different materials, NSCD@DFNS (pristine), NSCD@DFNS + BMB, NSCD@DFNS@BMB-AO, and NSCD@DFNS@BMB-AO@Au.

fluorescence emission (Fig. 4A and D). This turn-on behavior was supported by the fluorescence lifetime experiments where initially the probe material displayed a fluorescence lifetime of τ = 2.94 ns (quantum yield ($\emptyset$) = 0.65), which was further increased to 3.83 ns ($\emptyset$ = 0.84) after the addition of gold ions validating turn-on response (Fig. 4C). To further substantiate our findings, we systematically examined the fluorescence behavior of the materials (Fig. 4D). It is observed that the NSCD@DFNS composite also displays strong fluorescence emission due to the absence of electron or energy transfer pathways (similar to the NSCD@DFNS@BMB-AO material). However, the addition of the BMB ligand into the NSCD@DFNS suspension resulted in significant fluorescence quenching, indicative of active PET processes (Fig. 4D). Notably, the fluorescence quenching was more pronounced in the final probe material (NSCD@DFNS@BMB-AO) due to the covalent attachment of the amidoximated ligand, with fluorescence emission recovering upon the introduction of gold ions. Moreover, no spectral shifts are detected in the emission profile, ruling out the potential for internal charge transfer (ICT). Also, no FRET is possible with Au^{3+} analytes. These results collectively confirm that the turn-off–on behavior is mainly driven by PET on and off mechanisms.

2.4 Aqueous adsorption studies

Apart from the excellent photophysical activity, the adsorption performance of the material towards gold ions was investigated in the batch mode experiments.[70] The adsorption experiments were performed under both light and dark conditions, considering the material's possible photoactive properties. Initial findings suggest that when exposed to broad day sunlight, the material (NSCD@DFNS@BMB-AO) can remove over 95% of Au^{3+} ions within 15 minutes, compared to 80% removal in the absence of light (Fig. S14, ESI†). Preliminary batch adsorption experiments were conducted at various uranium concentrations (20 to 200 ppm) under light and dark conditions (Fig. 5), involving vigorous shaking for approximately 3 hours, followed by centrifugation, filtration, and analysis *via* ICP-MS. The equilibrium adsorption capacity (Q_e) was calculated using the formula $Q_e = (C_i - C_f)V/W$, where C_i and C_f are the initial and final concentrations of uranium ions, respectively, and V and W represent the volume and weight of the adsorbent, respectively. Following the Langmuir adsorption model, the adsorption isotherm plot revealed a maximum adsorption capacity (Q_e) of 780 mg g^{-1} and 550 mg g^{-1} under light and dark conditions (Fig. 5A, B, Table 2 and Fig. S15, ESI†). A competitive extraction study (30 ppm mix cations) revealed the excellent extraction behaviour of the material in the complex pool of ions (Table S2, ESI†). The higher adsorption capacity of gold ions under light conditions can be probably due to the synergistic effects of surface functional groups + strong binding by the amidoxime group and the photocatalytic action by NSCDs. Additionally, the OH functionality may have contributed to secondary coordination sphere effects, such as hydrogen bonding interactions and charge stabilization due to its electron-donating property revealing the high performance of the material. The adsorption performance at a larger scale (2 g) of the material was also investigated with 40 ppm gold

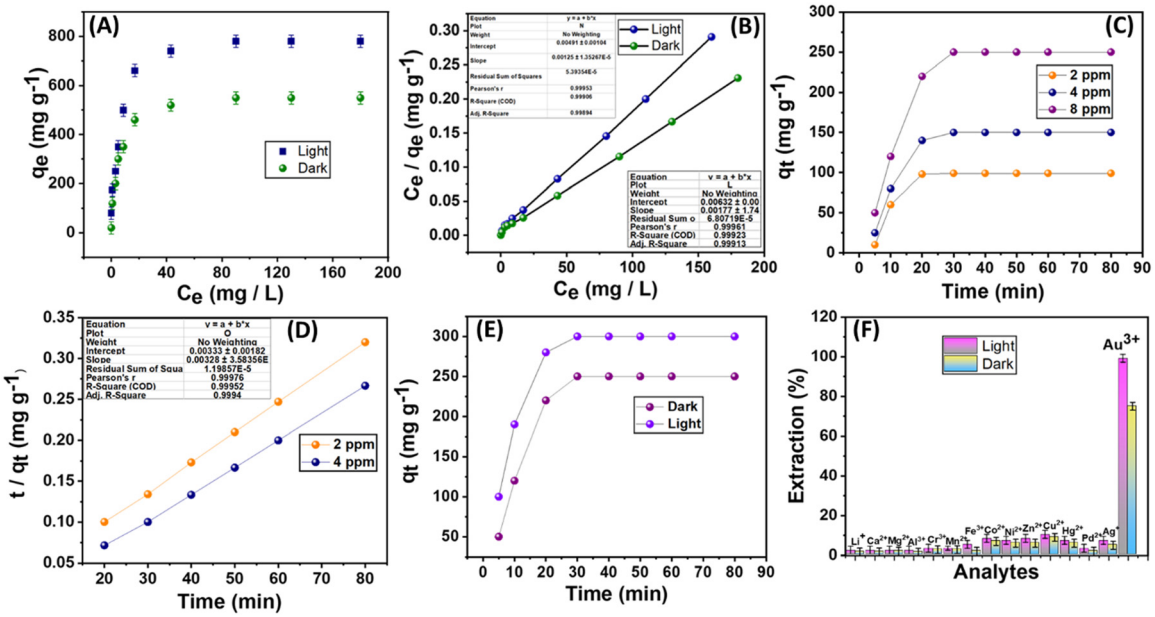

Fig. 5 (A) The experimental equilibrium adsorption capacity (q_e). (B) The Langmuir adsorption isotherm of the material towards Au^{3+} ions under light and dark conditions. (C) and (D) The sorption capacity (q_t) and pseudo-second-order kinetic plot towards gold concentrations (2, 4, and 8 ppm). (E) The sorption capacity plot of the material towards 8 ppm gold concentration under light and dark conditions; and (F) the competitive performance of the material in the 10-ppm spiked Au in mixed metal cations under light and dark conditions.

Table 2 The gold adsorption parameters towards Au^{3+} ions

Analyte	Experimental q_e (mg g^{-1})	Langmuir linear isotherm			Freundlich adsorption isotherm		
		q_{max} (mg g^{-1})	K_L (L g^{-1})	R^2	K_F	n	R^2
Au^{3+} (light)	780	800	0.706	0.99	0.376	0.281	0.945
Au^{3+} (dark)	550	564	0.280	0.99	0.357	0.384	0.953

solution, exhibiting a drastic colour change observed within 25 min of exposure evidenced by HR-TEM showing blockage of the fibrous pore channels (Fig. S16, ESI†).

2.5 Adsorption kinetics and thermodynamic aspects

Motivated by the impressive gold adsorption capabilities of the material in aqueous environments, we further investigated the kinetic parameters. To investigate the rate kinetics parameters, 10 mg of the material was immersed in 500 mL of various gold concentrations of 2, 4, and 8 ppm. Remarkably, the material exhibited high removal efficiency across varying concentrations, achieving removal rates exceeding 90% within 15 and 20 min towards concentrations of 2, 4, and 8 ppm, respectively. The corresponding gold uptake values were measured at 99, 145, and 250 mg g^{-1} for these specific concentrations (Fig. 5C and D). Motivated by the material's exceptional activity, a kinetics study was conducted at 8 ppm gold concentration under light and dark conditions. The material exhibited removal rates exceeding 95% within 20 minutes, with a notable ~20% difference in adsorption capacity between both conditions (Fig. 5E). Moreover, the adsorption rate was also assessed using pseudo-first-order and pseudo-second-order kinetic models. The equations for these models were carefully analyzed, with the pseudo-second-order model showing a close alignment between predicted and experimental values, indicating a high correlation factor (R^2) approaching unity. The linear relationship observed in the plots of t/q_t *vs.* t further suggests the chemical adsorption of gold (Fig. 5D, E and Fig. S17, ESI†).[65] Additionally, the material demonstrated excellent selectivity in the presence of coexisting ions, 10 ppm Au spiked in mix cations (Fig. 5F). To evaluate the impact of pH on adsorption, the extraction efficiencies of the material were assessed under varying pH conditions. The results indicate that the material maintains strong extraction efficiency across acidic, neutral, and basic environments, with peak performance observed in the pH range of 7 to 9 (Fig. S18, ESI†). However, at lower pH values, reduced extraction efficiency may result from quenching of photogenerated electrons by H^+ ions, potentially impacting photocatalytic activity. At very high pH, decreased efficiency may be attributed to competition from hydroxide ions, which can lead to the formation of insoluble gold hydroxide species, thereby hindering the extraction process.

The gold adsorption was also evaluated at different temperatures (298, 303, 308, 313, 318, and 323 K) to assess the thermodynamic parameters keeping other factors constant.[65,71] With the increase in temperature we have observed a simultaneous increase in equilibrium adsorption capacity from 50 at 298 K to 199 mg g^{-1} at 323 K, indicating a positive effect of temperature on the adsorption behaviour. This observation possibly suggests that the adsorption of gold ions is endothermic in nature with a positive influence of temperature. Moreover, we have determined ΔH, ΔS and ΔG parameters

Table 3 The thermodynamic parameters towards gold adsorption

Analyte	ΔH (kJ mol^{-1})	ΔS (kJ mol^{-1})	ΔG (kJ mol^{-1}) 298	303	308	313	318	323
Au^{3+}	206.80	0.70	−2.50	−6.0	−9.5	−13.0	−16.5	−20.05

using van't Hoff equation ($\log(q_e/C_e) = \Delta S/2.303R - \Delta H/2.303RT$) and Gibbs free energy ($\Delta G = \Delta H - T\Delta S$). In these equations, ΔH and ΔS are the enthalpies (J mol^{-1} K^{-1}) and entropy change (J mol^{-1} K^{-1}), R is the universal gas constant (8.314 J mol^{-1} K^{-1}), ΔG is Gibbs free energy and q_e/C_e is the adsorption affinity. The enthalpy (ΔH) and entropy (ΔS) changes were determined from the slope and intercept of the plot $\log(q_e/C_e)$ *vs.* $1/T$, which were found to be 206.80 and 0.70 kJ mol^{-1}, and thereafter ΔG values were calculated using the equation giving negative values, suggesting that the adsorption process was spontaneous and favourable (Fig. S19, ESI† and Table 3).

Apart from sensitive detection parameters and excellent adsorption performance of the material, the regeneration and reusability of the material are inevitable, offering sustainable and economic benefits. The material was successfully regenerated using thiourea (0.8 M) solution and tracked using fluorimetry; also, the reusability was studied up to 5 cycles. Initially, the removal performance fell by 2–3% due to structural changes, possibly due to the consecutive adsorption–desorption by the eluent and the bound residual gold ions to the functionality present in the material; however, the performance was maintained after the 3rd cycle (Fig. S20, ESI†). The regenerated material was thoroughly characterized using SEM, FTIR, and fluorescence, with morphology, functionality, and optical response resembling that of the original material (Fig. S21, ESI†).

2.6 Mechanism of sunlight enabled gold extraction

To study the photo-enhanced extraction behavior of the material towards gold, we systematically evaluated the XPS and PXRD spectra before and after the gold adsorption (Fig. 6). The full scan XPS spectra of the gold adsorbed material show the presence of Au 4f peaks, indicating the successful adsorption of gold ions (Fig. 6A). Upon further analysis, the O 1s and N 1s core–shell XPS spectra (Fig. S22, ESI†) of the gold adsorbed material showed a shift of ~0.2 eV along with new peaks at 531.7 and 398.7 eV corresponding to the O–Au and N–Au interactions, evidencing the strong gold interaction and adsorption. To gain further insights into the photocatalytic reduction process, the valence state distribution of gold ions under illuminated and dark conditions was quantitatively analyzed using XPS spectra. Under dark conditions, the core-level Au 4f spectra displayed peaks at 87.6 and 91.1 eV, corresponding to Au(III) $4f_{7/2}$ and $4f_{5/2}$, as well as peaks at 85.2 and 89.0 eV, attributed to Au(I) $4f_{7/2}$ and $4f_{5/2}$. Notably, no Au(0) peaks were detected. In contrast, the sample exposed to sunlight showed strong signals at 84.1 and 88.0 eV, corresponding to Au(0) $4f_{7/2}$ and $4f_{5/2}$, along with weaker peaks of Au(I) at 85.2 and 89.0 eV, confirming the occurrence of photocatalytic reduction (Fig. 6B and C). The photocatalytic reduction efficiency was estimated using the relative area of the $4f_{7/2}$ peaks due to their higher intensity, narrower FWHM (full-width at half maximum), and greater sensitivity compared to $4f_{5/2}$, yielding an efficiency of approximately 85% (Table S3, ESI†). Similarly, the PXRD spectra of the gold adsorbed material performed under light conditions showed peaks of metallic gold at 38.2°, 44.4°, 64.6°, and 77.5° corresponding to (111), (200), (220), and (311) planes and for the silica framework at 22.73° (Fig. 6D). This process initially involves the adsorption of gold ions Au(III) coupled with the photocatalytic reduction to Au(0) in the presence of sunlight by photogenerated electrons at the materials interface due to photoactive N,S doped carbon dots in the matrix. Doping nitrogen (N) and sulfur (S) into carbon dots greatly enhances their ability to absorb sunlight and generate photoinduced charge carriers, thereby improving their efficiency in chemical reduction processes. These dopants create new energy levels in the band structure, expanding the absorption spectrum to include visible light. This results in better separation and transfer of photogenerated electron–hole pairs, reducing recombination rates and extending charge carrier lifetimes. Furthermore, N and S doping increases the generation of reactive oxygen species (ROS), which are essential for photocatalytic reactions. These enhancements allow the doped carbon dots to utilize a wider spectrum of light for more efficient photocatalysis, facilitating continuous regeneration of active sites and maintaining long-term chemical reduction efficiency. The presence of photocurrents was further evaluated by various techniques such as transient photocurrents, electrochemical impedance spectra, and photoluminescence spectra. The band gap energies derived from the Tauc plots[54,58] of the UV-vis spectra of the starting material NSCD@DFNS and the final material NSCD@DFNS@BMB-AO were found to be 1.70 and 1.47 eV (Fig. 6E). The narrower band gap in the final material implies faster and easier conduction of photogenerated electrons viable for the photoreduction process of Au(III) to Au(0), also the valence band and the conduction band were determined to be +1.10 and −0.37 eV respectively. The redox potential of Au(III) to Au(0) (1.00 eV *vs.* NHE) lies in between the conduction (E_{CB}) and the valence band (E_{VB}) of the material implying the thermodynamic feasibility of the reduction process by the photogenerated electrons (Fig. 6F). The steady-state and lifetime spectra indicate the presence of higher photocurrent in the final material stating enhanced charge transfer and reduced recombination rates (electron–hole) implying excellent photocatalytic efficiency (Fig. 6G). The higher photocurrent was further confirmed by the EIS and photocurrent density data showing a higher current in the final material (NSCD@DFNS@BMB-AO) (Fig. 6H and I). Additionally, the positive surface field at the material interface created due to the released photoelectrons has a strong interaction with the $AuCl_4^-$ creating new adsorption sites and further enhancing adsorption and photocatalytic performance. Insightfully, the final material NSCD@DFNS@BMB-AO acts as an excellent heterojunction interface for the higher adsorption and efficient photocatalytic reduction of Au(III) to Au(0).

The N,S-doped carbon dots in the silica matrix can generate reactive oxygen species (ROS) under light irradiation, such as hydroxyl radicals and superoxide ions, which are highly reactive

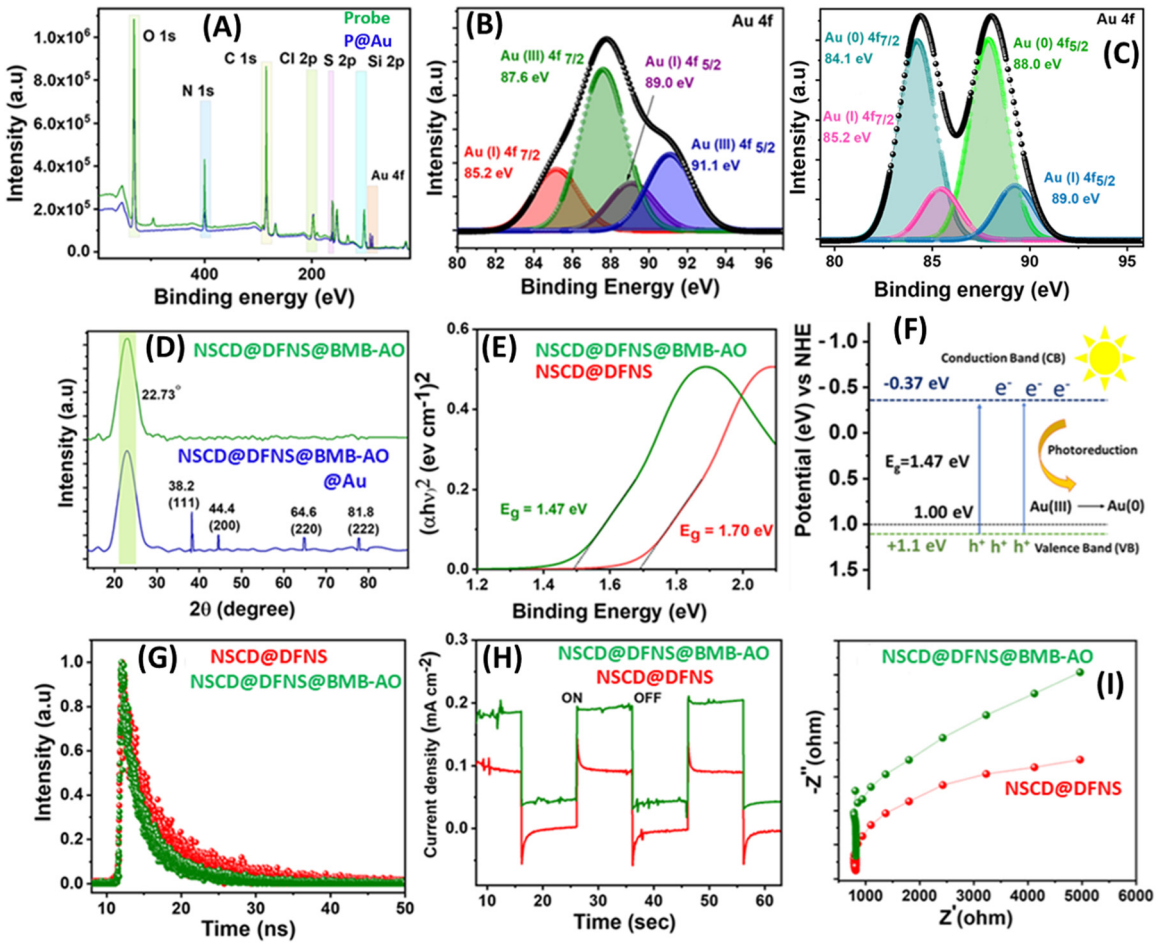

Fig. 6 (A) The XPS full scan spectra of the final material before and after gold adsorption. (B) The core–shell 4f spectra of the gold adsorbed material under dark conditions. (C) The core–shell 4f-XPS spectra of the gold adsorbed material under light conditions. (D) The comparison of the PXRD spectra of the material before and after gold adsorption under light conditions; (E) and (F) the UV-vis derived Tauc plot of the materials and the schematic plot of the photocatalytic redox potential of Au(III) to Au(0). (G) The photoluminescence lifetime spectra of the materials; and (H)–(I) the plot of comparison of the transient photocurrent response and the impedance plot of the materials.

and effective against bacteria.[72] Therefore, to study the antimicrobial effect due to probable ROS generation under light irradiation, the antibacterial activity has been tested against Gram-positive (*Bacillus subtilis*) and Gram-negative (*Pseudomonas aeruginosa*) bacterial strains under light and dark conditions by the broth dilution method.[73,74] It is observed that under light conditions, the material showed excellent antibacterial activity (98%) with minimum effects under the dark conditions (Fig. S23A, ESI†). This is probably due to the production of ROS reactive oxygen species under light conditions contributing to the excellent efficacy of the material against these bacterial strains (Fig. S23B, ESI†). The ROS produced by N,S-doped carbon dots can penetrate bacterial cell walls, causing oxidative damage to cellular components and ultimately leading to bacterial death. The generation of ROS was confirmed by electron paramagnetic resonance spectroscopy (ESR), where the final material NSCD@DFNS@BMB@AO in the presence of light showed signals of superoxide radicals, hydroxy radicals, and singlet oxygen, whereas no such signals were detected under dark conditions (Fig. S24, ESI†). The remarkable antibacterial activity of the final material due to ROS generation shows the anti-biofouling properties of the material, which helps sustain challenges of the complex environments. To better evaluate the performance of our material, we compared its properties with those reported in the literature (Table S4, ESI†).

2.7 Gold extraction from e-waste

Extraction experiments were performed to evaluate the extraction performance and practical viability of the material in real samples such as end-of-life electronic materials (e-waste). To begin with, ~150 gold chips were crushed and ground to increase the surface area and were soaked in 800 mL of aqua regia solution for 48 h. The presence of probable elements in the leachate was mapped using EDX analysis, showing the presence of Au, Co, Ni, and Cu (Fig. S25, ESI†). ICP-MS was used to analyze the leachate giving solution concentrations of 10.43 ppm for Au, 600 ppm for Cu, 200 ppm for Co, and 240 ppm for Ni. Afterward, the leachate was treated with 200 mg of the material and equilibrated for 3 h of adsorption. Subsequently, the material was recovered from the leached liquor and put inside 200 mL of thiourea solution for 4 h for Au striping. As a result, the striping solution becomes yellow in

colour and the material is regenerated and recovered. This process was repeated 3 times to extract any residual gold. The removal efficiency was monitored using ICP-MS and shows that 98% of gold is extracted while among other metals only Cu is also extracted (~3%), indicating selective adsorption of gold (Fig. S26 and 27, ESI†).

3. Conclusion

Conclusively, this study presents a rationally designed N,S co-doped carbon dot (NSCD)-encapsulated dendritic silica composite, which upon functionalization acts as a single platform for the simultaneous gold-ion detection and adsorption. The growth of NSCDs enables fluorescence emissions in the near IR-region and promotes the photoreduction of Au^{3+} to elemental gold with ROS-mediated antimicrobial activity. The designing strategy leads to turn-on detection of gold ions, where the photoelectron transfer (PET) from amidoxime to NSCDs leads to fluorescence quenching of the material, which, upon binding to the gold ions, the PET process breaks down, leading to recovery of the fluorescence emission (turn-on). This turn-off–on response and excitation-independent behaviour of the composite material towards gold ions in the near-IR region is relatively rare in the literature, which is advantageous for sensing applications. The material also displayed excellent adsorption capacity with fast kinetics, which was enhanced in the presence of light due to the photocatalytic effect of NSCDs. When applied to real samples, the material selectively extracts gold from e-waste leachates and shows high removal efficiency, highlighting its potential for practical applications.

Author contributions

Sanjay Yadav: conceptualization, methodology, investigation, data validation, writing original draft, formal analysis; Nishu Choudhary: methodology, data curation, formal analysis; Vasavdutta Sonpal: biological studies, data validation; Alok Ranjan Paital: conceptualization, writing – reviewing and editing, funding acquisition, formal analysis, supervision.

Conflicts of interest

The authors declare no competing financial or personal relations that could influence the work reported here.

Data availability

The data supporting this article have been included as part of the ESI.†

Acknowledgements

S. Y., N. C., V. S., and A. R. P. acknowledge the Council of Scientific Industrial Research (CSIR), Govt. of India for the financial support. AcSIR is acknowledged for providing a PhD degree and ADCIF-CSIR for instrumentation analytical facilities. The CSIR-CSMCRI communication number is 90/2025.

References

1 E. D. Doidge, I. Carson, P. A. Tasker, R. J. Ellis, C. A. Morrison and J. B. Love, *Angew. Chem., Int. Ed.*, 2016, **55**, 12436–12439.
2 B. Zhu, S. Gong and W. Cheng, *Chem. Soc. Rev.*, 2019, **48**, 1668–1711.
3 R. Kerrich, *Science*, 1999, **284**, 2101–2102.
4 Y. Wei, W. Zhang and J. Gao, *Green Chem.*, 2024, **26**, 5684–5707.
5 J. Luo, X. Luo, M. Xie, H.-Z. Li, H. Duan, H.-G. Zhou, R.-J. Wei, G.-H. Ning and D. Li, *Nat. Commun.*, 2022, **13**, 7771.
6 R. L. Manley, E. Alonso and N. T. Nassar, *Resour. Policy*, 2022, **78**, 102889.
7 E. Williams, *Nature*, 2011, **479**, 354–358.
8 V. R. Moreira, E. A. Torres, J. C. Balarini and M. C. S. Amaral, *Chem. Eng. J.*, 2023, **476**, 146906.
9 A. Lapresta-Fernández, A. Fernández and J. Blasco, *TrAC, Trends Anal. Chem.*, 2012, **32**, 40–59.
10 Y. Pan, A. Leifert, D. Ruau, S. Neuss, J. Bornemann, G. Schmid, W. Brandau, U. Simon and W. Jahnen-Dechent, *Small*, 2009, **5**, 2067–2076.
11 M. Enea, E. Pereira, M. Peixoto de Almeida, A. M. Araújo, M. de, L. Bastos and H. Carmo, *Nanomaterials*, 2020, **10**, 995.
12 A. Scheffer, C. Engelhard, M. Sperling and W. Buscher, *Anal. Bioanal. Chem.*, 2008, **390**, 249–252.
13 L. Kocúrová, I. S. Balogh, J. Škrlíková, J. Posta and V. Andruch, *Talanta*, 2010, **82**, 1958–1964.
14 S. Singha, D. Kim, H. Seo, S. W. Cho and K. H. Ahn, *Chem. Soc. Rev.*, 2015, **44**, 4367–4399.
15 J. Luo, X. Luo, M. Xie, H.-Z. Li, H. Duan, H.-G. Zhou, R.-J. Wei, G.-H. Ning and D. Li, *Nat. Commun.*, 2022, **13**, 7771.
16 D. Mei and B. Yan, *Angew. Chem.*, 2024, **63**, e202402205.
17 N. Ren, H. Lan, W. Guan, Y. Liu, L. Gu, Y. Mao and L. Wang, *Sens. Actuators, B*, 2023, **378**, 133156.
18 Z. Chen, D. Wang, S. Feng and H. Liu, *ACS Appl. Mater. Interfaces*, 2021, **13**, 23592–23605.
19 T. L. Mako, J. M. Racicot and M. Levine, *Chem. Rev.*, 2019, **119**, 322–477.
20 K. D. Hakkel, M. Petruzzella, F. Ou, A. van Klinken, F. Pagliano, T. Liu, R. P. J. van Veldhoven and A. Fiore, *Nat. Commun.*, 2022, **13**, 103.
21 M. Mohamed, A. K. Klenke, M. V. Anokhin, H. Amadou, P. J. Bothwell, B. Conroy, E. E. Nesterov and I. V. Nesterova, *ACS Sens.*, 2023, **8**, 1109–1118.
22 Y. Chen, M. Xu, J. Wen, Y. Wan, Q. Zhao, X. Cao, Y. Ding, Z. L. Wang, H. Li and Z. Bian, *Nat. Sustainable*, 2021, **4**, 618–626.
23 A. K. Awasthi, J. Li, L. Koh and O. A. Ogunseitan, *Nat. Electron.*, 2019, **2**, 86–89.
24 M. Koide, V. Hodge, E. D. Goldberg and K. Bertine, *Appl. Geochem.*, 1988, **3**, 237–241.

25 L. M. M. Kinsman, B. T. Ngwenya, C. A. Morrison and J. B. Love, *Nat. Commun.*, 2021, **12**, 6258.
26 S. S. M. Vance, M. Mojsak, L. M. M. Kinsman, R. Rae, C. Kirk, J. B. Love and C. A. Morrison, *Inorg. Chem.*, 2024, **63**, 9332–9345.
27 Y. Su, A. Berbille, X.-F. Li, J. Zhang, M. PourhosseiniAsl, H. Li, Z. Liu, S. Li, J. Liu, L. Zhu and Z. L. Wang, *Nat. Commun.*, 2024, **15**, 4196.
28 I. G. B. N. Makertihartha, M. Zunita, Z. Rizki and P. T. Dharmawijaya, *AIP Conf. Proc.*, 2017, **1805**, 030008.
29 R. Sharma, N. F. Suhendra, S.-H. Jung and H. Lee, *Chem. Eng. J.*, 2023, **451**, 138506.
30 D. T. Sun, N. Gasilova, S. Yang, E. Oveisi and W. L. Queen, *J. Am. Chem. Soc.*, 2018, **140**, 16697–16703.
31 Z. Chang, L. Zeng, C. Sun, P. Zhao, J. Wang, L. Zhang, Y. Zhu and X. Qi, *Coord. Chem. Rev.*, 2021, **445**, 214072.
32 M. Soleimani and T. Kaghazchi, *Bioresour. Technol.*, 2008, **99**, 5374–5383.
33 M. Huy Do, G. Tien Nguyen, U. Dong Thach, Y. Lee and T. Huu Bui, *Miner. Eng.*, 2023, **191**, 107977.
34 Z. Dong, J. Liu, W. Yuan, Y. Yi and L. Zhao, *Chem. Eng. J.*, 2016, **283**, 504–513.
35 S. W. Won, P. Kotte, W. Wei, A. Lim and Y.-S. Yun, *Bioresour. Technol.*, 2014, **160**, 203–212.
36 D. Majumder, S. Fajal, M. M. Shirolkar, A. Torris, Y. Banyla, K. Biswas, S. Rasaily and S. K. Ghosh, *Angew. Chem., Int. Ed.*, 2025, **64**, e202419830.
37 J. Zhao, Z. Qiao, Y. He, R. Zhang, H. Li, X. Song, D. Cao and S. Wang, *Angew. Chem., Int. Ed.*, 2025, **64**, e202414366.
38 M. Liu, D. Jiang, Y. Fu, G. Zheng Chen, S. Bi, X. Ding, J. He, B. Han, Q. Xu and G. Zeng, *Angew. Chem.*, 2024, **63**, e202317015.
39 D. Jiang, Z.-L. Wang, Y.-Z. Cheng, Y.-X. Yu, H.-Y. Kong, X.-Y. Bian, X.-M. Dou, S.-L. Li, D.-H. Yang, X. Ding and B.-H. Han, *Chem. Eng. J.*, 2024, **497**, 154212.
40 T. Xue, T. He, L. Peng, O. A. Syzgantseva, R. Li, C. Liu, D. T. Sun, G. Xu, R. Qiu, Y. Wang, S. Yang, J. Li, J.-R. Li and W. L. Queen, *Sci. Adv.*, 2023, **9**, eadg4923.
41 Y. Xiang, C.-Y. Cheng, M.-H. Liu, W.-C. Bai, Z.-X. Zang, L. Xu, Y. Yu and G.-J. Liu, *Sep. Purif. Technol.*, 2024, **335**, 126131.
42 J. Feng, W. Jiang, Z. Tang, K. Shi, H. Jiang, L. Zhang, M. Zhou and S. Chen, *Colloids Surf., A*, 2024, **703**, 135241.
43 J. Ren, Q. Li, Z. Zhu, Y. Qiu, F. Yu, T. Zhou, X. Yang, K. Ye, Y. Wang, J. Ma and J. Zhao, *Small*, 2024, **20**, 2404241.
44 Z. Chang, F. Li, X. Qi, B. Jiang, J. Kou and C. Sun, *J. Hazard. Mater.*, 2020, **391**, 122175.
45 X. Zhang, H. Li, Z. Liu, Z. Fu, H. Zhang, G. Wang and Y. Zhang, *ACS ES&T Eng.*, 2024, **4**, 2403–2414.
46 X. Li, Y.-L. Wang, J. Wen, L. Zheng, C. Qian, Z. Cheng, H. Zuo, M. Yu, J. Yuan, R. Li, W. Zhang and Y. Liao, *Nat. Commun.*, 2023, **14**, 263.
47 T. S. Nguyen, Y. Hong, N. A. Dogan and C. T. Yavuz, *Chem. Mater.*, 2020, **32**, 5343–5349.
48 R. Ding, Y. Chen, Y. Li, Y. Zhu, C. Song and X. Zhang, *ACS Appl. Mater. Interfaces*, 2022, **14**, 11803–11812.
49 W. Zhang, C. Liu, X. Meng, J. Sun and H. Tian, *Chem. Eng. J.*, 2024, **489**, 151246.
50 A. Haleem, Y. Pan, F. Wu, M. Ullah, S. Chen, H. Li and J. Pan, *Sep. Purif. Technol.*, 2024, **345**, 127305.
51 H. Dong, G. Shang, Y. Zhang, E. Dai, M. Shao, C. Chen, H. He, Z. Nie, M. Xiong, D. Miao and S. Zhao, *Molecules*, 2024, **29**, 2398.
52 J. Shi, S. Peng, B. Kuang, S. Wang, Y. Liu, J. Zhou, X. Li and M. Huang, *Adv. Mater.*, 2024, **36**, 2405731.
53 K. R. Kim, S. Choi, C. T. Yavuz and Y. S. Nam, *ACS Sustainable Chem. Eng.*, 2020, **8**, 7359–7370.
54 Q. Wang, M. Unno and H. Liu, *J. Mater. Chem. A*, 2024, **12**, 5679–5691.
55 W.-R. Cui, Y.-R. Chen, H.-F. Wei, X.-Y. Fan and Y. Li, *Sep. Purif. Technol.*, 2025, **354**, 129263.
56 L. Zhao, Q. Zhou, Y. Yang, Y. Zhang, Y. Qiu, Y. Chen, X. Jin, X. Yang and S. Wang, *J. Water Process Eng.*, 2024, **57**, 104572.
57 Z. Feng, H. Fu, Z. Wang, F. Wang, Y. Wei, C. Zhao and C.-C. Wang, *Sep. Purif. Technol.*, 2024, **351**, 128102.
58 S. Yadav, N. Choudhary, V. Sonpal, B. G. Vyas and A. R. Paital, *J. Mater. Chem. A*, 2025, **13**, 3858–3871.
59 D. Mei and B. Yan, *Small*, 2023, **19**, 2304811.
60 L. Zhang, J.-Q. Fan, Q.-Q. Zheng, S.-J. Xiao, C.-R. Zhang, S.-M. Yi, X. Liu, W. Jiang, Q.-G. Tan, R.-P. Liang and J.-D. Qiu, *Chem. Eng. J.*, 2023, **454**, 140212.
61 V. Polshettiwar, D. Cha, X. Zhang and J. M. Basset, *Angew. Chem., Int. Ed.*, 2010, **49**, 9652–9656.
62 V. Polshettiwar, *Acc. Chem. Res.*, 2022, **55**, 1395–1410.
63 A. Maity, R. Belgamwar and V. Polshettiwar, *Nat. Protoc.*, 2019, **14**, 2177–2204.
64 S. Yadav, N. Choudhary, M. Ranjan Dash and A. Ranjan Paital, *Chem. Eng. J.*, 2022, **450**, 138042.
65 S. Yadav, N. Choudhary, V. Sonpal and A. Ranjan Paital, *Chem. Eng. J.*, 2023, **471**, 144715.
66 K. Holá, M. Sudolská, S. Kalytchuk, D. Nachtigallová, A. L. Rogach, M. Otyepka and R. Zbořil, *ACS Nano*, 2017, **11**, 12402–12410.
67 Y. Liu, H. Wang, X. Yuan, Y. Wu, H. Wang, Y. Z. Tan and J. W. Chew, *Chem. Catal.*, 2021, **1**, 44–68.
68 K. J. Mintz, Y. Zhou and R. M. Leblanc, *Nanoscale*, 2019, **11**, 4634–4652.
69 S. Yadav, N. Choudhary and A. R. Paital, *Carbon*, 2023, **205**, 527–539.
70 S. Chatterjee and A. R. Paital, *Adv. Funct. Mater.*, 2018, **28**, 1704726.
71 N. Choudhary, S. Yadav, T. R. Patel, P. D. Wakchaure, V. Sonpal, B. Ganguly and A. R. Paital, *J. Mater. Chem. A*, 2024, **12**, 27340–27354.
72 M. Maruthapandi, A. Saravanan, P. Das, J. H. T. Luong and A. Gedanken, *Biotechnol. Adv.*, 2021, **53**, 107843.
73 P. Li, L. Sun, S. Xue, D. Qu, L. An, X. Wang and Z. Sun, *SmartMat*, 2022, **3**, 226–248.
74 N. H. Hussen, A. H. Hasan, Y. M. FaqiKhedr, A. Bogoyavlenskiy, A. R. Bhat and J. Jamalis, *ACS Omega*, 2024, **9**, 9849–9864.